Supplementary information to the manuscript:

Highly conductive grain boundaries in cold-sintered barium zirconate-based proton conductors

Moritz Kindelmann[1,2,3,*], Sonia Escolastico[4], Laura Almar [4], Ashok Vayyala[1,2], Dylan Jennings[2,3], Wendelin Deibert[3], Wilhelm Albert Meulenberg[3], Wolfgang Rheinheimer[3], Martin Bram[3], Jose Serra[4,*], Joachim Mayer[1,2], Olivier Guillon[3,5,*]

[1] RWTH Aachen University, Central Facility for Electron Microscopy (GFE), 52074 Aachen, Germany

[2] Forschungszentrum Jülich GmbH Ernst Ruska-Centre for Microscopy and Spectroscopy with Electrons (ER-C), 52425 Jülich, Germany

[3] Forschungszentrum Jülich GmbH, Institute of Energy and Climate Research, Materials Synthesis and Processing (IEK-1), 52425, Jülich, Germany

[4] Instituto de Tecnología Química, Universitat Politècnica de València-Consejo Superior de Investigaciones Científicas, 46022, Valencia, Spain

[5] Jülich Aachen Research Alliance, JARA-Energy, 52425, Jülich, Germany

Corresponding authors:

m.kindelmann@fz-juelich.de

jmserra@itq.upv.es

o.guillon@fz-juelich.de

Microstrucutre development after thermal post treatments (TPT)

To understand the influence of thermal post-treatments on the microstrucutre development after cold sintering, a systematic variation between 1100 °C and 1600 °C has been conducted. Representative microstrucutres are displayed in Fig. S1. Temperatures at 1100 °C are not sufficent to reform the phase which can also be observed in the fine and porous microstructure. The stepwise increase of annealing temperatures leads to higher densities as well as a increase in grain size. Annealing at temperatures from 1500 °C show a comparable microstrucutre to samples produced by SSRS, which can be associated with

the solution of residual NiO and the formation of the SSRS specific transient BaY_2NiO_5 phase that promotes grain growth.

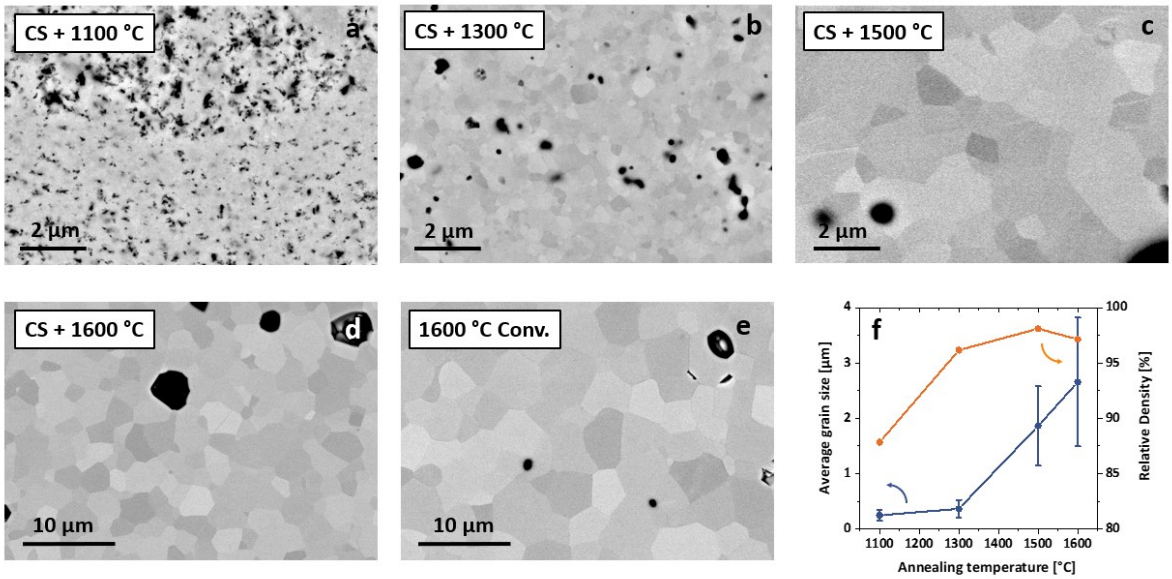

Figure S1: Microstructure development after thermal post treatments. Representative cross-sectional SEM images of TPT samples treated at (a) 1100 °C, (b) 1300 °C, (c) 1500 °C and (d) 1600 °C. For comparison the microstructure of a conventional processed sample at 1600°C is also shown (e). Additionally, figure 1g is reprinted here (f) to add information on the relative density and average grain size (derived from EBSD measurements) of the shown microstructures.

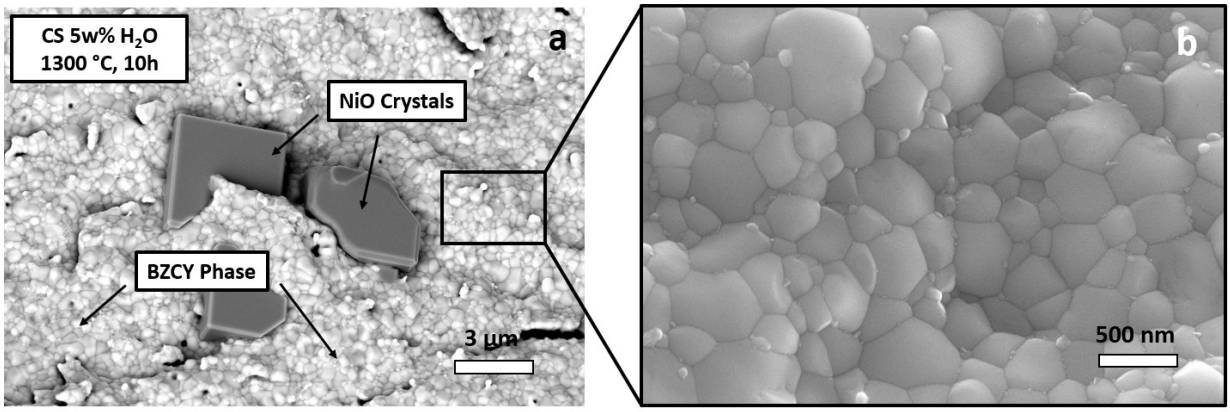

Figure S2: Overview of the microstructure of TPT1300 samples. (a) SEM image of a fracture surface of TPT 1300 sample showing embedded NiO crystals. (b) Higher magnification SEM image of the nano-grained BZCY microstructure.

The presence of NiO in TPT1300 samples could not be shown using XRD due to the very low amounts present in the applied powders. However, low amounts of embedded NiO crystals can be found in SEM images of fracture surfaces made from samples annealed at 1300 °C (Fig. S2 a).

The NiO secondary particles clearly show that our processing approach can prevent the formation of a transient BaY_2NiO_5 phase improving the electrochemical performance of fine-grained BZCY, which was processed at comparably low temperatures.

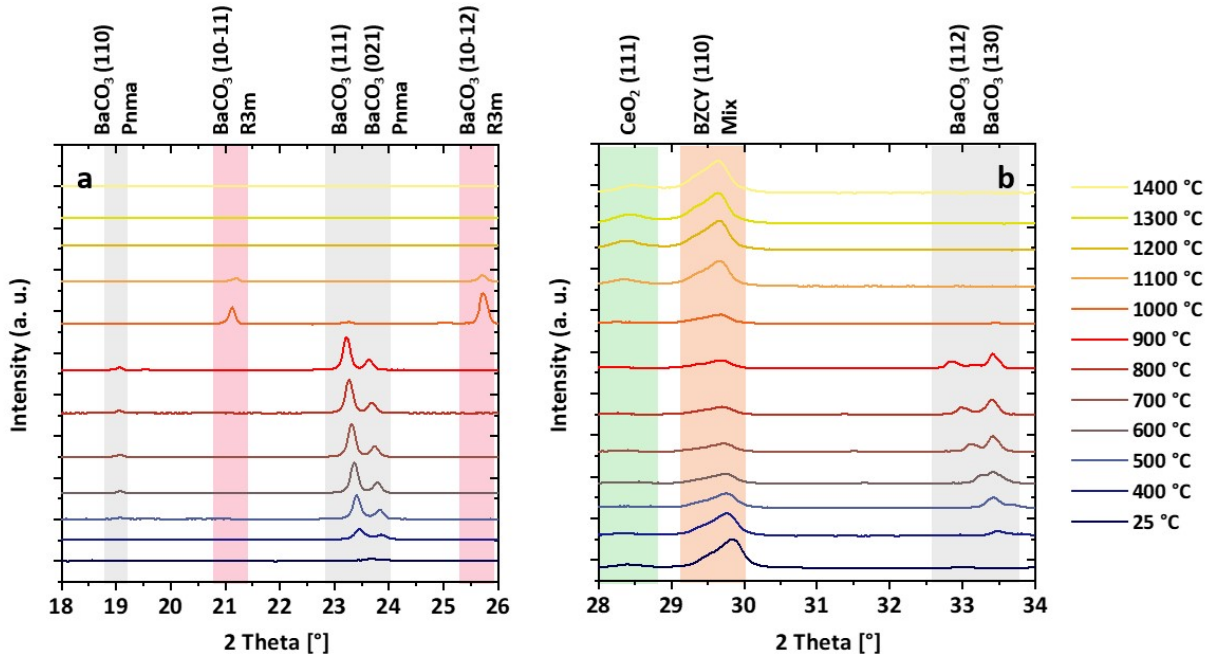

Figure S3: HT-XRD measurements highlighting the in-situ phase changes during thermal annealing. (a) Section of the diffractogram from 18 – 26 ° highlighting the formation and decomposition of $BaCO_3$. (b) Section of the diffractogram from 28 – 34 ° showing the (110) peak of the BZCY phase as well as CeO_2 and $BaCO_3$ secondary phases.

Additional to ex-situ XRD investigations, which are included in the main manuscript, a HT-XRD study was performed to investigate the reformation process of the perovskite phase after cold sintering. The heating rate and holding times at every temperature are 5 K/min and 1h, respectively. A downside of these measurements is that they are not suitable to reproduce the real annealing cycle applied in the main study, where a constant heating rate to high temperatures and an extended dwell time of 10 h is applied. Additionally, decomposition processes are observed at the surface of the measured pellet during in-situ XRD reducing the significance for bulk processes. Additionally, the temperature measurement in the applied setup has a mismatch of around 100 K due to thermal conduction through the sample. However, several processes that are also discussed

in the main text can be observed here: (1) Formation of $BaCO_3$ from $Ba(OH)_2$ species in the pellet beginning at 400 °C. The formation is associated with a simultaneous decrease of the BZCY perovskite peak intensity. (2) Phase change of the $BaCO_3$ Pnma phase to the high temperature R3m phase between 900 and 1000°C and the subsequent decomposition of $BaCO_3$ above 1100°C. (3) Formation of a clear CeO_2 (111) signal at 28.3° at temperatures above 1100 °C. The HT-XRD investigations clearly support the reaction pathway that is described in the manuscript. Despite the mismatch between the thermal history of the HT-XRD and the TPT applied in the main study (the solution of CeO_2 and Y_2O_3 into the perovskite phase cannot be tracked), important additional information can be derived from these experiments.

Electrochemical characterization and conductivity performance benchmark

In the following, additional electrochemical data is presented and detailed to highlight the performance of low temperature processed BZCY in comparison to its conventionally processed counterpart. Fig. S4 shows an extended figure including additional EIS data of the TPT1500 sample (a-c) and exemplary raw data measurements of TPT1300 and CONV1600 (d-f). Even though the TPT1500 sample has been exposed to higher temperatures and experienced a decent amount of grain growth the electrochemical performance is still comparable to TPT1300. Slight changes in the activation energy might be associated to a different chemistry at the grain boundary after complete solution of NiO and other residual phases like Y_2O_3.

Furthermore, exemplary EIS measurements (in Fig S4 d and e) highlight the strong differences between the electrochemical response of low temperature and conventional processed BZCY. Through our novel processing route, the grain boundary resistivity plays a minor role in the total conductivity of the BZCY electrolyte. The bulk conductivity of both samples however is in a comparable range.

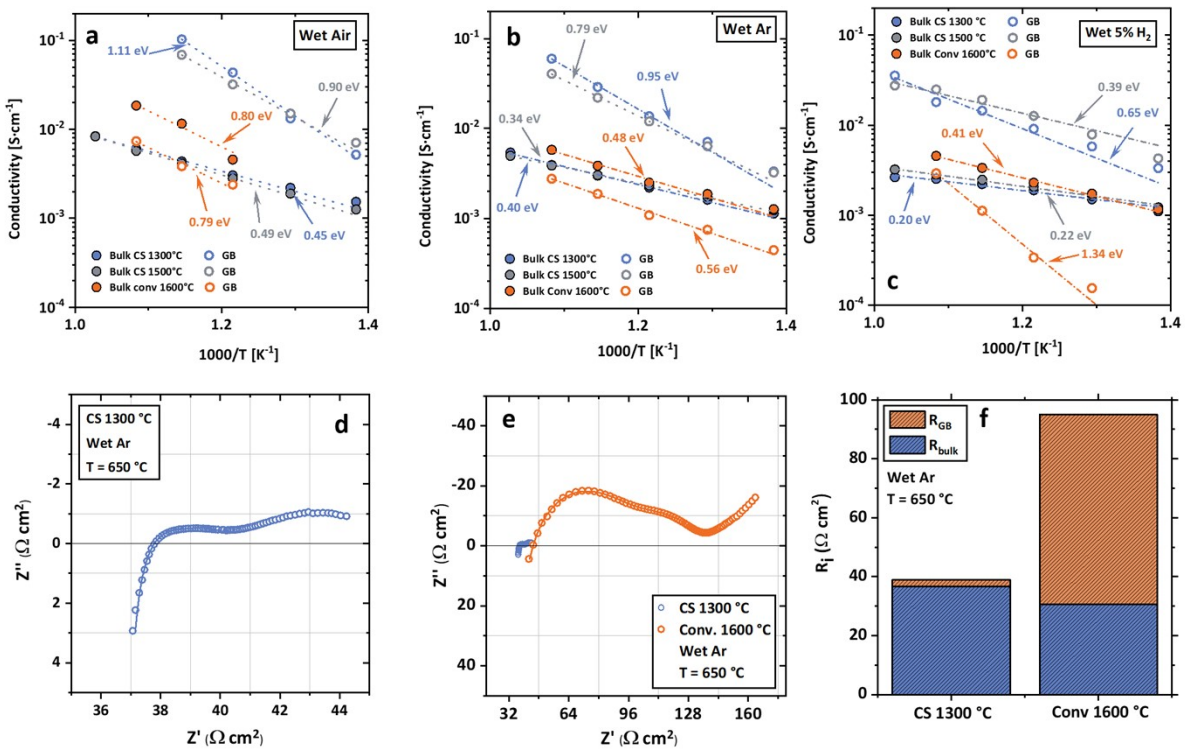

Figure S4: Extended electrochemical impedance data of low-temperature processed BZCY. Electrochemical impedance spectroscopy (EIS) of CONV (1600 °C, 5 h), TPT1300 (1300 °C, 10 h) and TPT1500 BCZY in wet air (a), wet Ar (b), and wet H_2 (c) (all 3% H_2O). Full circles represent the bulk conductivity, and empty circles represent the grain boundary conductivity. (d) Nyquist plot of a EIS measurement of TPT1300 at 650 °C in wet Ar and a comparison graph including the same measurement of a CONV1600 sample (e). (f) Comparing the bulk and grain boundary conductivity of the measurements shown in (d, e).

Next to the measurement of the H/D isotopic effect in wet reducing atmospheres, comparable investigations were made in dry Ar and wet Ar (H_2O and D_2O). BZCY electrolytes processed through our new low temperature route reveal a very comparable performance to conventionally sintered BZCY. The TPT temperature has no visible effect on the measured conductivity in all three atmospheres, which additionally highlights the neglectable influence of grain boundaries in cold sintered and thermally treated BZCY (especially in TPT1300 where a high grain boundary density is present).

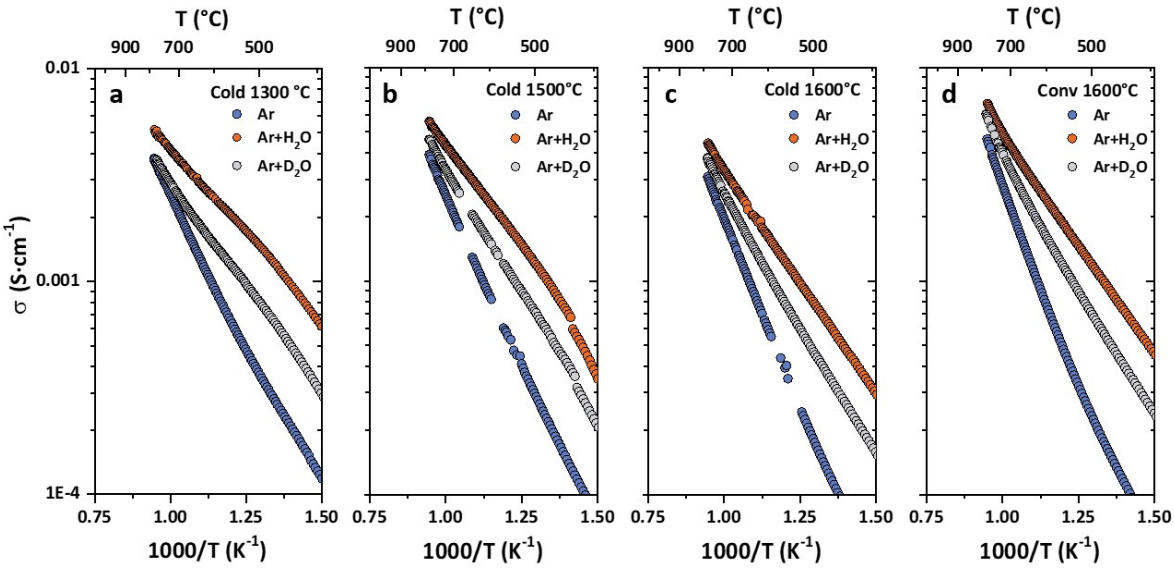

Figure S5: H/D effect on the conductivity measurements in Ar atmosphere. DC conductivity of different BZCY samples in dry and wet Ar (3% H_2O and 3% D_2O). (a) TPT1300, (b) TPT1500, (c) TPT1600 and (d) CONV1600.

The total conductivity at 600 °C is used as a benchmark value in Fig. 3f comparing it to the maximal sintering temperature and sintering technique. In Fig. S6 and Tab. S1 the literature sources as well as additional details on the composition and test conditions are given.

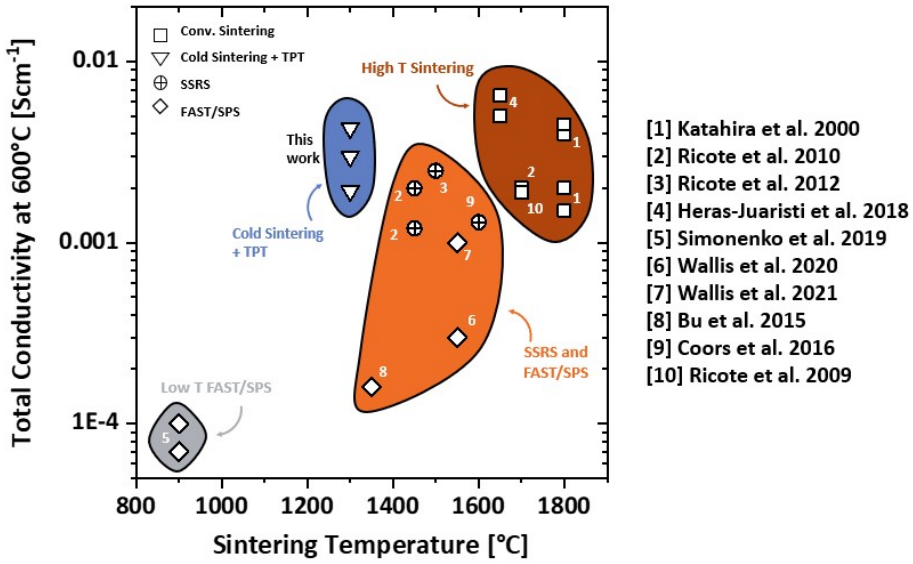

Figure S6: Performance benchmark of low-temperature processed BZCY. The total conductivity at 600 °C is correlated to the maximal sintering temperature. Additionally, the applied sintering technique is highlighted through different colors and markers.

Table S1: Literature overview of conductivity values at 600 °C of Zr-rich BZCY compositions.

Material	Method	Sintering T [°C]	Sintering time [h/min]	Sintering aid [w%]	Conductivity at 600 ° [S/cm]C	Atmosphere	Reference
BZCY63	Conventional	1800	5 h	---	0,002	wet H_2 pH_2O $1.7x10^3$	[1]
BZCY81	Conventional	1800	5 h	---	0,0015	wet H_2 pH_2O $1.7x10^3$	[1]
BZCY63	Conventional	1800	5 h	---	0,004	wet air pH_2O $1.7x10^3$	[1]
BZCY81	Conventional	1800	5 h	---	0,0045	wet air pH_2O $1.7x10^3$	[1]
BZCY72	Conventional	1700	6 h	---	0,002	wet H_2N_2 (9%), pH_2O = 0.015 atm	[2]
BZCY72	SSRS	1450	6 h	1 Ni	0,002	wet H_2N_2 (9%), pH_2O = 0.015 atm	[2]
BZCY72	SSRS	1450	6 h	2 Ni	0,0012	wet H_2N_2 (9%), pH_2O = 0.015 atm	[2]
BZCY72	SSRS	1500	4 h	1 Ni	0,0025	wet 9% H_2 in N2 (0.015 atm H_2O)	[3]
BZCY72	Conventional	1650	4-8 h	---	0,005	wet N_2	[4]
BZCY72	Conventional	1650	4-8 h	---	0,0065	wet air	[4]
BZCY81	SPS	900	5 min	---	0,00007	atmosphere air	[5]
BZCY63	SPS	900	5 min	---	0,0001	atmosphere air	[5]
BZCY72	SPS	1550	5 min	---	0,0003	wet %5H_2/Ar	[6]
BZCY72	SPS	1550	5 min	---	0,001	5% H_2, 3 kPa H_2O	[7]
BZCY72	SPS	1350	5 min	---	0,00016	Wet H_2	[8]
BZCY72	SSRS	1600	16 h	1 Ni	0,0013	5% H_2, 3 kPa H_2O	[9]
BZCY72	Conventional	1700	6 h	---	0,0019	9% H_2, 1.5 kPa H_2O	[10]
BZCY72	Cold sintering + TPT	1300	10 h	0.5 Ni	0,004	3% H_2O air, Ar, H_2	This work

Atom Probe Tomography

In Fig. 4c of the main manuscript a cropped version of the data complete APT dataset is shown. Fig. S7 displays the full dataset of the measured APT needle, including three grain boundaries highlighted through the Y and Ni segregation as well as a Y_2O_3 secondary phase grain. The already discussed Ce heterogeneity is clearly visible in the overview image and the grain boundary proxigrams (Fig. S7 b, c). Additionally, segregation phenomena at the heterointerface between BZCY and the Y_2O_3 secondary phase can be observed.

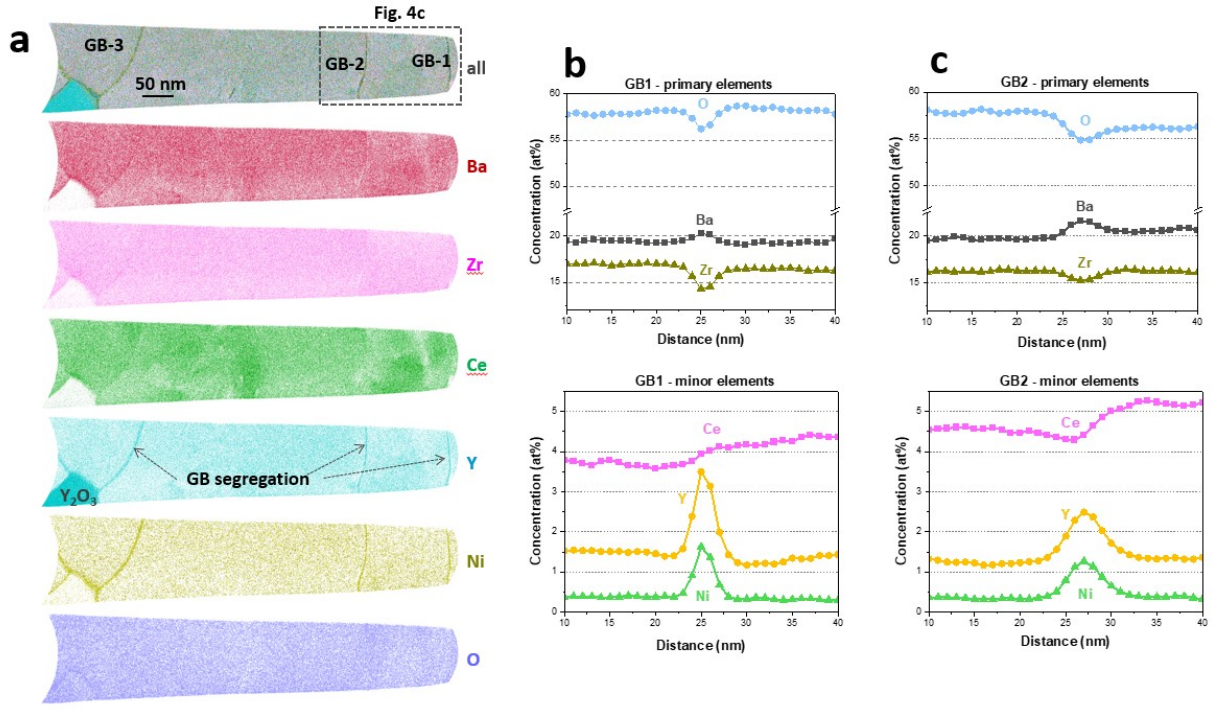

Figure S7: Atom probe tomography of interfaces in the TPT1300 BZCY sample. (a) Full data set of the measured APT needle highlighting the detail that is used in Fig. 4c. The nano-crystallinity of the sample enables a simultaneous measurement of three GBs. (b, c) Line scans derived from grain boundary 1 and 2 showing comparable characteristics.

References

1 K. Katahira, Y. Kohchi, T. Shimura and H. Iwahara, *Solid State Ionics*, 2000, **138**, 91–98.

2 S. Ricote and N. Bonanos, *Solid State Ionics*, 2010, **181**, 694–700.

3 S. Ricote, N. Bonanos, A. Manerbino and W. G. Coors, *Int. J. Hydrogen Energy*, 2012, **37**, 7954–7961.

4 G. Heras-Juaristi, U. Amador, R. O. Fuentes, A. L. Chinelatto, J. Romero De Paz, C. Ritter, D. P. Fagg, D. Pérez-Coll and G. C. Mather, *J. Mater. Chem. A*, 2018, **6**, 5324–5334.

5 T. L. Simonenko, M. V. Kalinina, N. P. Simonenko, E. P. Simonenko, O. V. Glumov, N. A. Mel'nikova, I. V. Murin, O. O. Shichalin, E. K. Papynov, O. A. Shilova, V. G. Sevastyanov and N. T. Kuznetsov, *Int. J. Hydrogen Energy*, 2019, **44**, 20345–20354.

6 J. Wallis, L. Urban, C. Grimmer, W. Bodnar, R. Zimmermann, S. Ricote, K. D. Weltmann, E. Burkel and A. Kruth, *Solid State Ionics*, 2020, **345**, 115118.

7 J. Wallis, S. Ricote, K. D. Weltmann, E. Burkel and A. Kruth, *Ceram. Int.*, 2021, **47**, 15349–15356.

8 J. Bu, P. G. Jönsson and Z. Zhao, *Scr. Mater.*, 2015, **107**, 145–148.

9 W. G. Coors, A. Manerbino, D. Martinefski and S. Ricote, *Perovskite Mater. Characterisation, Prop. Appl.*, 2016, 84–106.

10 S. Ricote, N. Bonanos and G. Caboche, *Solid State Ionics*, 2009, **180**, 990–997.